Stirring Coherence Time to Predict Stirrer Efficiency in Loaded Reverberation Chambers

Andréa Cozza

Stirring Coherence Time to Predict Stirrer Efficiency in Loaded Reverberation Chambers

Andrea Cozza, *Senior Member, IEEE*

***Abstract*—The last two decades have seen numerous investigations about the optimal design of mechanical stirrers for reverberation chambers (RC), with the aim of improving their stirring efficiency, without leading to a clear consensus on the reasons for their limited efficiency. This paper introduces a new criterion, by focusing on the incremental disorder introduced by mechanical stirrers, measured by their stirring coherence time, a measure of the rate of loss of coherence independent from the RC loading and excitation source. The model predicts that increasing losses would result in a loss of disorder, and therefore of stirring efficiency. Therefore, the stirring efficiency is not limited by a stirrer being too small (electrically) or too simple-shaped, but by the limited time they have to introduce disorder in a lossy RC. Experimental tests confirm the accuracy of the model's predictions under variable loading conditions. The model can predict the maximum loading for which a stirrer can be acceptably efficient. It applies to EMC testing of lossy devices, as well as over-the-air (OTA) tests for wireless communication devices, where absorbers are introduced in order to emulate different propagation environments.**

***Index Terms*—Reverberation chambers, mechanical stirrers, stirring efficiency, chamber loading, EMC tests, over-the-air tests, auto-correlation function, image principle, transport theory, wave diffusion.**

I. Introduction

The operation of reverberation chambers (RCs) is based on the two main requirements: the generation of a complex field distribution resulting in uniform testing conditions within its working volume and the ability to alter this distribution in order to create a large number of random testing configurations, ideally uncorrelated [1], [2]. This second requirement is fulfilled by means of stirring techniques [3], with mechanical stirrers ranking among the most popular solutions. An important figure of merit for stirrers is the stirring efficiency, which is typically defined as the ratio between the effective number N_e of uncorrelated (ideally independent) field or power samples generated by the stirrer, out of $N \geq N_e$ configurations generated. Multiple methods exist for estimating N_e/N, e.g. [4], [5], among which the auto-correlation function (ACF) of the samples generated by the stirrer is widely applied [1], [2].

A wide body of work in the literature has investigated how the stirring efficiency depends on the stirrer electrical dimensions and shape, resulting in the proposal for many solutions with complex shapes [6]–[16]. Yet, there is currently no clear explanation about what physical mechanisms limit the stirring efficiency. Furthermore, the stirring efficiency has been shown to be affect by the RC loading conditions [5], [17]–[22], which makes the performance of a stirrer more difficult to compare, also forcing RC users to repeat tests under different loading conditions in order to assess its apparently variable efficiency.

Recent work has investigated the use of the total scattering cross section of the stirrer as a means for assessing its stirring efficiency [23]–[25], using the method proposed in [26], based on the estimation of the *stirrer damping time*, which measures the rate of diffusion generated by the stirrer. A notable advantage of this method is that it is independent from the RC loading. But while the ability of a stirrer to diffuse energy is indeed fundamental, it does not provide any direct information about its stirring efficiency.

This paper proposes a new method for characterizing the stirring efficiency of mechanical stirrers, independent from the RC loading conditions and capable of accurately predicting how the stirring efficiency degrades when an RC is loaded, by monitoring the ACF of the stirrer response in time domain.

Crucially, the proposed model explains what limits the stirring efficiency in simple, intuitive terms. The model is based on the following idea: as a scatterer of finite electrical dimensions, stirrers can only scatter a fraction of the coherent energy radiated by an antenna. Multiple successive interactions will further lead to stronger diffusion and, most importantly, an accrued sensitivity of the resulting field distribution to the position of the stirrer, which would translate into a increasingly different field distribution. But because of dissipation phenomena, the late-time interactions with the stirrer will be increasingly attenuated, and therefore have a vanishingly low chance of making a difference in the overall field distribution. Inevitable losses are therefore the reason why stirrers have limited efficiency, while a stirrer operating in a less dissipative RC would perform better. In other words, losses act as a sort of loose time gating, weighing down the more complex late-time response of a stirrer.

The paper is organized as follows. We first discuss about the modeling of a stirrer impact on wave propagation within an RC, using two complementary approaches: multi-path propagation modeling and transport theory. The stirring efficiency is shown to depend on the *stirring coherence time*, a fundamental figure of merit measuring how quickly the stirrer can reduce the coherence of impinging waves. The stirring coherence time enables quantitative predictions of the stirring efficiency, which is shown to have a different origin than the stirrer damping time. Sec. III elaborates on this notion, deriving a very simple predictive model of the stirring efficiency for a loaded RC. Extensive experimental results are reported in Sec. IV, confirming the accuracy of the proposed model. Finally, Sec. V discusses the practical implications of our findings, in

A. Cozza is with the Group of Electrical Engineering - Paris (GeePs), CentraleSupelec, Univ. Paris-Sud, Université Paris-Saclay, Sorbonne Universités, UPMC Univ Paris 06, 3 & 11 rue Joliot-Curie, Plateau de Moulon 91192 Gif-sur-Yvette CEDEX, France (email: andrea.cozza@ieee.org).

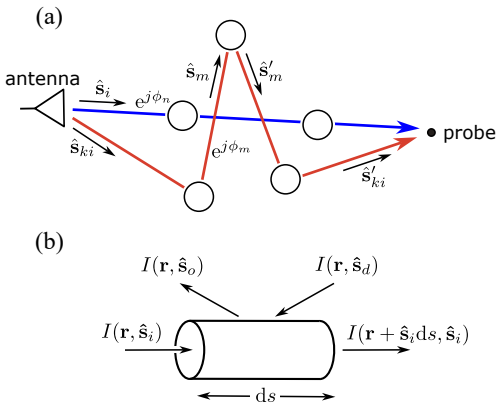

Fig. 1: Propagation through diffusive media: (a) multi-path trajectories between individual scatterers, (b) transport theory equilibrium of intensities in an element of length $\mathrm{d}s$.

particular how the proposed model can be used for predicting the impact of an RC loading on a stirrer efficiency and the maximum loading that would degrade the stirrer efficiency to an acceptable degree. While Sec. II may appear abstract, it is fundamental in order to understand why a new metric quantifying the stirrer efficiency is needed and justify why the stirring coherence response obeys an exponential decay. For the Reader less keen on theory but interested in the practical aspects of the proposed model, it is possible to skip Sec. II entirely, taking the result (15) as a working assumption.

II. Transport Theory for Mechanical Stirring

The objective of this section is twofold: first, to explain why the time-domain ACF (tACF) of stirrer-generated samples follows an exponential decay; second, to show that the tACF time constant and the stirring damping time have different origins. To this end, we will need to work jointly on two complementary models, in order to explain the macroscopic behavior of stirrers, starting from their free-space scattering characteristics. The goal is not to develop a rigorous predictive model, but rather to meet the two goals mentioned above.

Propagation in mode-stirred RCs involves multiple scattering events, requiring appropriate propagation models. Fig. 1(a) shows an example of a wave propagating through multiple identical scatterers before reaching a probe. This scenario can be described by a multipath propagation model, where the wave propagation is explained in terms of the superposition of all possible propagation paths between a source (an antenna) and a probe, passing through scatterers [27]. One path, shown in blue in Fig. 1, stands out of all the others as it connects the source to the probe along a straight line, potentially interacting with scatterers along the way, which will be referred to as the forward-propagating or line-of-sight path. The other paths may include a very large number of scattering sequences, involving back-and-forth interactions between the scatterers.

Each path originates from free-space radiation from the antenna, described as a spherical wave weighted by the antenna gain pattern. Interaction with the scatterers is described by their scattering function $f(\hat{\mathbf{s}}_m,\hat{\mathbf{s}}'_m)$, measuring how a local plane wave impinging along the direction $\hat{\mathbf{s}}_m$ is scattered along the outgoing direction $\hat{\mathbf{s}}'_m$, subject to spherical attenuation and propagation phase shift. The signal at the probe output at the frequency ν can then be written as the sum of the contributions of each propagation path

$$x(\nu)=\sqrt{G_t(\hat{\mathbf{s}}_i)G_r(\hat{\mathbf{s}}_i)}m_p\prod_n \mathrm{e}^{\mathrm{j}\phi_n}d_n^{-1}f(\hat{\mathbf{s}}_i,\hat{\mathbf{s}}_i)+ \\ +\sum_k\sqrt{G_t(\hat{\mathbf{s}}_{ki})G_r(\hat{\mathbf{s}}'_{ki})}m_{ki}\prod_m \mathrm{e}^{\mathrm{j}\phi_m}d_m^{-1}f(\hat{\mathbf{s}}_m,\hat{\mathbf{s}}'_m) \tag{1}$$

where $G_t(\hat{\mathbf{s}})$ and $G_r(\hat{\mathbf{s}})$ are the source antenna and probe gains along the generic direction $\hat{\mathbf{s}}$, ϕ_n is the propagation phase shift between two scatterers and d_n their distance; m is the polarization match at the probe for each path. In the following, the attenuations d_n^{-1} will be dropped, for the sake of compactness, since when moving to transport theory spherical attenuation is taken into account indirectly. The first term in (1) describes the forward-propagating path.

A radically different approach is applied in transport theory, describing the spatial evolution of the average intensity[1] of the overall field distribution, as evaluated at a position $\boldsymbol{r}$ propagating along the direction $\hat{\mathbf{s}}_i$. To do so, it establishes a differential equation describing at what rate the forward-propagating intensity is scattered, and finally diffused, along other directions and how part of this diffuse intensity would also be reoriented along the forward-propagation direction (see Fig. 1(b)). For scatterers with total cross section σ_t and volume density n, the resulting differential equation reads [27]

$$\frac{\mathrm{d}}{\mathrm{d}s}I(\boldsymbol{r},\hat{\mathbf{s}}_i)=-n\sigma_t I(\boldsymbol{r},\hat{\mathbf{s}}_i)+\int_{4\pi}\mathrm{d}\hat{\mathbf{s}}_d|f(\hat{\mathbf{s}}_d,\hat{\mathbf{s}}_i)|^2I(\boldsymbol{r},\hat{\mathbf{s}}_d) \tag{2}$$

where the first term in the right-hand side represents the rate of intensity diffused away from the incoming direction $\hat{\mathbf{s}}_i$, while the integral represents the amount of diffuse intensity (i.e., along all directions) redirected along $\hat{\mathbf{s}}_i$.

As argued in Sec. II-B, only the forward-propagating intensity I_f scattered along the incident direction $\hat{\mathbf{s}}_i$ matters in the analysis of the stirring efficiency. For a isotropic and homogeneous multi-scattering medium (2) yields [27]

$$I_f(s)=I_{f,o}\mathrm{e}^{-n\sigma_t s} \tag{3}$$

with the forward-propagating intensity exponentially decaying at it propagates through a multi-scattering medium. In general $\sigma_t=\sigma_a+\sigma_d$, with σ_a the absorption cross section σ_a, measuring how much power is dissipated by the scatterer, and only σ_d measuring the power it diffuses along all directions.

Since I_f propagates along a single well-defined direction, the distance s it travels along can be mapped into the time of arrival at the probe

$$I_f(t)=I_{f,o}\mathrm{e}^{-n\sigma_t ct}=I_{f,o}\mathrm{e}^{-t/\tau_d}\mathrm{e}^{-t/\tau_a} \tag{4}$$

with c the speed of light. The time constant τ_d is the *diffusion time*, measuring how quickly the forward-propagating intensity is converted into diffuse intensity. This model has been applied to the characterization of mechanical stirrers in the last decade [23]–[25], where τ_d was referred to as the *stirrer damping*

[1] i.e., the power density per steradian.

time, in order to estimate the stirrer total scattering cross section.

While it is clear that the ability to generate a diffuse field is important for RC applications, the diffusion time does not measure the ability of the stirrer to generate statistically uncorrelated diffuse configurations, i.e., to efficiently stir the field distribution, as it rotates. Indeed, a large total scattering cross section can also be expected for large and complex-shaped equipments under test (EUTs), ensuring a rapid diffusion. Still, they would hardly be expected to be good candidates for efficient mechanical stirring.

The remained of this section lays the ground for the introduction of a new figure of merit for stirrers, capable of quantitatively predicting the ability of a stirrer to efficiently modify the diffuse field distribution within an RC, the *stirring coherence time*, which is shown in Sec. III to be able to accurately predict how the stirrer efficiency is affected by the RC loading conditions.

A. Image-based propagation model

The classical transport-theory model (3) is based on open-media propagation, and does not acknowledge the peculiar conditions imposed by RCs, with multiple reflections playing a fundamental role in field diffusion.

A simple and effective approach to model wave propagation in RCs as if evolving in open space is through the image principle. This approach is widely used in acoustics to better understand reverberation [28], and has more recently been extended to electromagnetic RCs [29]. These models have focused on empty RCs, and have proved that indeed diffusion is generated even without stirrers, with acoustics defining a diffusion time for an empty RC, known as mixing time [30].

For the case where a scatterer is included, it is no longer sufficient to introduce a periodic grid of source images, but it is also necessary to include a similar grid of scatterer images. This need can be understood from Fig. 2, where stirrer images model propagation paths where a wave interacts with the stirrer before being reflected by a wall. Fig. 2(a) considers a straight path between one of the antenna images and a probe (blue line), with only forward-scattering interactions with stirrer images, which correspond to multiple passages through the stirrer in the actual RC (red line). This kind of path corresponds to the forward-propagating path expected in multi-scattering propagation, shown in Fig. 1(a) in Sec. II. On the contrary, Fig. 2(b) considers an indirect path where a wave reaches the probe after multiple lateral scattering events (blue line) between stirrer images, which corresponds to a sequence of reflection and stirrer scattering events (red line). This case corresponds to the multi-scattering path in Fig. 1(a). These two examples also show that the stirrer images must be flipped in order to account for the correct relative orientation between the stirrer and the direction of propagation of the path.

It appears therefore that propagation through a RC with a mechanical stirrer differs from the standard scenario expected for transport theory by two aspects: 1) the overall signal received by the probe is the resultant of individual contributions generated by each source image, each providing a forward-propagating path and a diffuse-field distribution from multiple-scattering through the stirrer images, as in (1). The forward-propagating contributions are sufficient to generate diffusive conditions, as shown in [29], but in presence of a stirrer they are complemented by the diffuse-field contributions generated by each source image; 2) propagation losses are not only explained by the absorption cross section σ_a of the stirrer, but also by additional losses from the RC walls. This last issue can be easily corrected a posteriori, by enforcing the exact power decay rate τ_a estimated from the RC composite Q factor.

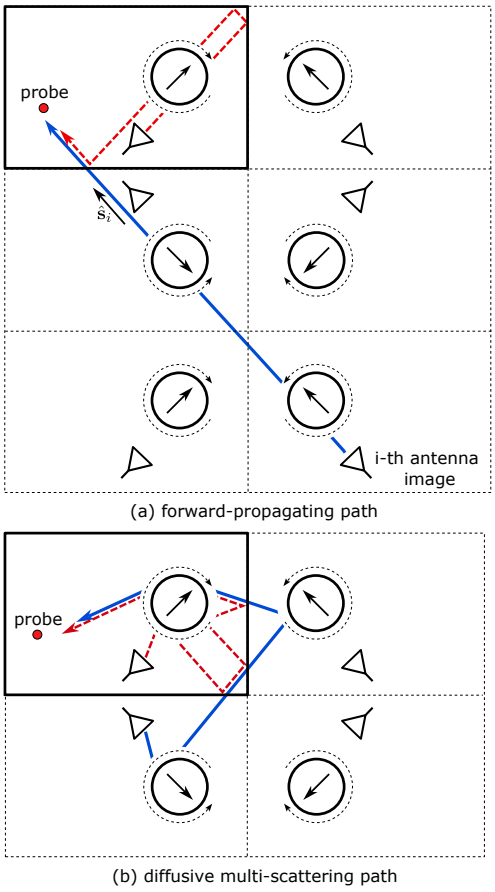

Fig. 2: Wave propagation within the proposed image model, where the actual RC is represented with a solid thick border, while the few images shown have dashed borders. The actual wave trajectory is shown as a dashed red line, while its equivalent trajectory in the image model is shown as a blue solid line. Two examples are shown: (a) a forward-propagating path and (b) a contribution characterized by several lateral scattering events from the stirrer.

Describing the contribution of each source image according to (1) and summing over all their contributions, the received signal $x(t;\psi)$ can be modeled as narrow-band excitation around the frequency ν using the analytic-signal notation

$$x(t;\psi) = \left\{ \sum_i \sqrt{G_t(\hat{\mathbf{s}}_i) G_r(\hat{\mathbf{s}}_i)} m_i \prod_n \mathrm{e}^{\mathrm{j}\phi_n} f_\psi(\hat{\mathbf{s}}_i, \hat{\mathbf{s}}_i) + \sum_{i,k} \sqrt{G_t(\hat{\mathbf{s}}_{ik}) G_r(\hat{\mathbf{s}}'_{ik})} m_{ik} \prod_m \mathrm{e}^{\mathrm{j}\phi_m} f_\psi(\hat{\mathbf{s}}_m, \hat{\mathbf{s}}'_m) \right\} \mathrm{e}^{-t/2\tau_a} \tag{5}$$

where f_ψ is the scattering pattern, as defined just before (1), for the stirrer positioned at an angle ψ.[2]

The average received power is therefore

$$\left\langle |x(t;\psi)|^2 \right\rangle_\psi = \left\{ \sum_i G_t(\hat{\mathbf{s}}_i) G_r(\hat{\mathbf{s}}_i) \left\langle |m_i|^2 \prod_n |f_\psi(\hat{\mathbf{s}}_i, \hat{\mathbf{s}}_i)|^2 \right\rangle_\psi + \sum_{i,k} G_t(\hat{\mathbf{s}}_{ik}) G_r(\hat{\mathbf{s}}'_{ik}) \left\langle |m_{ik}|^2 \prod_m |f_\psi(\hat{\mathbf{s}}_m, \hat{\mathbf{s}}'_m)|^2 \right\rangle_\psi \right\} \mathrm{e}^{-t/\tau_a} \tag{6}$$

where the contributions from cross-product terms do not appear, as they result in an incoherent summation, i.e., they present randomly distributed phase differences, thus averaging out to zero, compared to the squared moduli appearing in (6). The first sum covers the forward-propagating paths between each source image and the probe, where scattering by stirrer images occur only along a single direction, including their flipped versions.

The stirrer scattering cross section σ_d would emerge from the terms $|f_\psi(\hat{\mathbf{s}}_i, \hat{\mathbf{s}}_i)|^2$ only if they were integrated over all possible incoming and outgoing directions, since [27]

$$\sigma_d = \frac{1}{4\pi} \int_{4\pi} \mathrm{d}\hat{s}_i \int_{4\pi} \mathrm{d}\hat{s}_o |f_\psi(\hat{\mathbf{s}}_i, \hat{\mathbf{s}}_o)|^2 = \frac{1}{4\pi} \int_{4\pi} \mathrm{d}\hat{s}_i \, \sigma_i(\psi) \tag{7}$$

which in fact does not appear in (6), since angular averages (over stirrer positions and propagation paths) apply to the products modeling the propagation along each path, instead of directly to $|f_\psi|^2$. We therefore refer to the result of these averages as $\sigma_i(\psi)$, representing the (partial) scattering cross section for a wave impinging along $\hat{\mathbf{s}}_i$, for the stirrer position ψ.

It is now possible to apply transport theory to each forward path, using (4) to model the products in the forward-propagating terms in the first summation in (6),

$$\begin{aligned} &\mathrm{e}^{-t/\tau_a} \sum_i G_t(\hat{\mathbf{s}}_i) G_r(\hat{\mathbf{s}}_i) \left\langle F(\hat{\mathbf{s}}_i) \mathrm{e}^{-n\sigma_i(\psi) s_i} \right\rangle_\psi \\ &= \mathrm{e}^{-t/\tau_a} \sum_i G_t(\hat{\mathbf{s}}_i) G_r(\hat{\mathbf{s}}_i) \left\langle F(\hat{\mathbf{s}}_i) \mathrm{e}^{-t/\tau_i(\psi)} \right\rangle_\psi \end{aligned} \tag{8}$$

where each forward-propagating path is thus described by decaying exponential functions of amplitude $F(\hat{\mathbf{s}}_i)$ and a decay set by the diffusion time $\tau_i(\psi)$ along the direction $\hat{\mathbf{s}}_i$, associated to $\sigma_i(\psi)$, for a stirrer angle ψ.[3] s_i is the distance between the i-th antenna image and the probe.

A stirrer is by definition not rotation invariant, therefore $\tau_i(\psi)$ can be expected to present significant differences over the stirrer position ψ and the direction $\hat{\mathbf{s}}_i$. The averaging over all stirrer orientations ψ smooths out the dependence from the direction $\hat{\mathbf{s}}_i$ only with respect to the azimuthal angle ϕ, (taking the stirrer rotation axis as a reference), but leaves out a potential dependence from the elevation angle ϑ of each path. The forward-propagating term in (8) would therefore be approximated as

$$\begin{aligned} &\mathrm{e}^{-t/\tau_a} \sum_i G_t(\vartheta_i, \varphi_i) G_r(\vartheta_i, \varphi_i) \bar{F}(\vartheta_i) \mathrm{e}^{-t/\bar{\tau}_p(\vartheta_i)} \\ &\simeq F_o \mathrm{e}^{-t/\tau_a} \mathrm{e}^{-t/\tau_d}, \end{aligned} \tag{9}$$

where the final approximation involves averaging across the decay functions of all forward-propagating paths.

This model corresponds to the diffusion model applied in [26], in order to estimate the scattering cross section σ_d of small scatterers in an RC from the diffusion time constant τ_d. In fact, this result indicates that within an RC there is no straightforward relationship between τ_d and the total scattering cross section of the stirrer defined in (7), but rather an averaging over the different diffusion-related decay functions for each forward-propagation path.

More important is the fact that the tenuous approximation used in [26] only holds for single scattering events [27], neglecting multi-scattering contributions, which is clearly incompatible with how stirrers affect wave propagation within RCs, where a diffusive regime is expected. Taking as an example the RC presented in Sec. IV, with $\tau_a \simeq 1$ μs, significant attenuation would be observed only after more than 500 m, covering more than 100 times the RC diagonal, resulting in a very thick three-dimensional grid of stirrer images around the probe. Nonetheless, τ_d is still useful for assessing the ability of a stirrer to scatter incident waves and therefore to rapidly generate a diffuse field.

Back to (6), the second term modeling stirrer-generated diffusion cannot be neglected, since it involves coherent sums. Since all dissipation phenomena are already modeled by $\exp(-t/\tau_a)$, the diffuse contribution must perfectly compensate the decay in the forward-propagating contributions [27], resulting in the well-known expression of the power-delay profile

$$P(t) = \left\langle |x(t;\psi)|^2 \right\rangle_\psi = P_o \mathrm{e}^{-t/\tau_a}. \tag{10}$$

B. Stirring coherence time

The previous derivation is a fundamental step in understanding the tACF of the stirrer-generated set of probe signals, which measures the rate of disorder introduced by the stirrer over time. The tACF will also be the starting point for deriving a model of the stirrer frequency-domain ACF (fACF) derived in Sec. III. We define the tACF as

$$R(t;k) = \frac{\left\langle x^\star(t;\psi) x(t;\psi_k) \right\rangle_\psi}{\left\langle |x(t;\psi)|^2 \right\rangle_\psi} \tag{11}$$

where $\psi_k = \psi + k\Delta\psi$, with k the stirrer sample lag for a stirrer step $\Delta\psi$ and $x(t;\psi)$ is assumed to have been zero-averaged, in order to limit the complexity of (11) and later expressions.

The time-domain evolution of the covariance at the numerator can be derived following the same steps applied in

[2] as discussed in the previous page, stirrer images are actually flipped, so incoming and outgoing directions should be expressed relative to their local reference system, but we will use the same symbols for the sake of simplicity.

[3] the responses of the flipped versions of the stirrer will also be included under this same term, for the sake of simplicity.

the analysis of the average received power for a narrow-band excitation, yielding

$$\begin{aligned}&\langle x^\star(t;\psi)x(t;\psi_k)\rangle_\psi = \\ &\mathrm{e}^{-t/\tau_a}\left\{\sum_i G_t(\hat{\mathbf{s}}_i)G_r(\hat{\mathbf{s}}_i)\left\langle|m_i|^2\prod_n C(\hat{\mathbf{s}}_i,\hat{\mathbf{s}}_i;\psi,k)\right\rangle_\psi + \right. \\ &\left.\sum_{i,k} G_t(\hat{\mathbf{s}}_{ik})G_r(\hat{\mathbf{s}}'_{ik})\left\langle|m_{ik}|^2\prod_m C(\hat{\mathbf{s}}_m,\hat{\mathbf{s}}'_m;\psi,k)\right\rangle_\psi\right\}\end{aligned} \tag{12}$$

with $C(\hat{\mathbf{s}}_i,\hat{\mathbf{s}}_o;\psi,k) = f^\star_\psi(\hat{\mathbf{s}}_i,\hat{\mathbf{s}}_o)f_{\psi_k}(\hat{\mathbf{s}}_i,\hat{\mathbf{s}}_o)$. The covariance is expected to converge towards a real quantity, as can be proven by following the derivation in the appendix of [31].

When comparing (12) to (6) the former can be interpreted as describing an equivalent propagation scenario with a scattering function $f^\star_\psi(\hat{\mathbf{s}}_i,\hat{\mathbf{s}}_o)f_{\psi_k}(\hat{\mathbf{s}}_i,\hat{\mathbf{s}}_o)$, where the signal coherence, as measured by the covariance $\langle x^\star(t;\psi)x(t;\psi_k)\rangle_\psi$, takes the place of the received power.

Compared to (6), these equivalent scattering events now result in a loss of coherence at each interaction, due to the change in the stirrer state. The impact of the stirrer change can be quantified by introducing the coherence loss $\rho(\hat{\mathbf{s}}_i,\hat{\mathbf{s}}_o;\psi,k)$

$$\begin{aligned}C(\hat{\mathbf{s}}_i,\hat{\mathbf{s}}_o;\psi,k) &= |f_\psi(\hat{\mathbf{s}}_i,\hat{\mathbf{s}}_o)|^2\frac{C(\hat{\mathbf{s}}_i,\hat{\mathbf{s}}_o;\psi,k)}{|f_\psi(\hat{\mathbf{s}}_i,\hat{\mathbf{s}}_o)|^2} \\ &= |f_\psi(\hat{\mathbf{s}}_i,\hat{\mathbf{s}}_o)|^2\rho(\hat{\mathbf{s}}_i,\hat{\mathbf{s}}_o;\psi,k),\end{aligned} \tag{13}$$

which is closely related to a correlation coefficient. Being evaluated only along one propagation path, ρ acts as a partial correlation, or better a projection, measuring the similarity between the stirrer scattering function for two stirrer positions.

Since $|\rho| \leq 1$, (13) implies that the scatterer has an equivalent absorption cross section $\sigma_c(k) = \sigma_d/\rho(k)$; the subscript c reminds that it represents coherence losses instead of power attenuation. Eq. (3) shows that an absorption cross section would result in an additional exponential decay term, and thus a faster decay as the partial correlation in (13) decreases.

Therefore, given a forward-propagating and a multi-scattering path arriving at the same time at the probe, the latter will present a loss of coherence, with a variable response depending on the directions $\hat{\mathbf{s}}_i$ and $\hat{\mathbf{s}}_o$ of each interaction, as opposed to the forward interactions where the optical theorem [27] ensures the same response for any direction $\hat{\mathbf{s}}_i$. The probe signal covariance (12) is therefore dominated by the forward-propagating contribution, as opposed to the variance, or average output power (6). Clearly, this approximation would no longer hold if the stirrer becomes ineffective, e.g., if electrically small or if rotation invariant, since in this case there would be no loss of coherence when the stirrer rotates.

Applying the transport theory solution for the forward-propagating contributions yields a solution sharing the same structure than (9)

$$\langle x^\star(t;\psi)x(t;\psi_k)\rangle_\psi \simeq R'_s(k)\mathrm{e}^{-t/\tau_s(k)}\mathrm{e}^{-t/\tau_a} \tag{14}$$

but with a time constant $\tau_s(k)$, the *stirring coherence time*, now controlled by the k-lag partial correlations of the stirrer scattering function, as opposed to the stirrer damping time which is instead controlled by the stirrer partial scattering cross sections. Because the covariance decay is now explained by both diffusion and coherence losses, $\tau_s(k)$ can be expected to be smaller than the diffusion time τ_d appearing in (9).

We finally obtain from (14) and (10)

$$R(t;k) = R_s(k)\mathrm{e}^{-t/\tau_s(k)} \tag{15}$$

independent from the RC losses. Naturally, as the stirrer lag $k > 1$ the coherence is expected to drop faster over time, because the stirrer angular covariance is expected to decrease.

The initial coherence $R_s(k)$ is of special interest, since it measures the coherence only involving single-scattering events from the very first stirrer images around the probe, along multiple combinations of impinging and outgoing directions. It can therefore be expected to represent an estimator of the angular ACF of the free-space scattering function of the stirrer, but this hypothesis would require an extensive numerical analysis to be confirmed. Moreover, since both $R_s(k)$ and $\tau_s(k)$ depend on the angular ACF of the stirrer scattering response, when $R_s(k)$ decreases also $\tau_s(k)$ should decrease.

It is worth reminding that these derivations are not meant to predict the stirrer coherence function from knowledge of the stirrer free-space scattering function, because of the shear complexity of the full expressions, as well as the difficulty in estimating all the data needed, especially the stirrer scattering function $f(\hat{\mathbf{s}}_i,\hat{\mathbf{s}}_o)$. But these models clarify the differences between the diffusion and the coherence time of a stirrer and predict an exponential decay in the tACF. Furthermore, they clearly indicate that RC losses should not have any impact on the stirring coherence functions studied in the next sections.

III. Frequency-domain stirring ACF

Starting from (15) it is possible to predict how propagation losses affect the fACF

$$R(\nu,k) = \frac{\langle x^\star(\nu;\psi)x(\nu;\psi_k)\rangle_\psi}{\left\langle|x(\nu;\psi)|^2\right\rangle_\psi} \tag{16}$$

with ν the frequency. Applying the Fourier transform to the numerator yields

$$\begin{aligned}&\langle x^\star(\nu;\psi)x(\nu;\psi_k)\rangle_\psi = \\ &= \int \mathrm{d}t_1\mathrm{e}^{\mathrm{j}\omega t_1}\int \mathrm{d}t_2\,\langle x^\star(t_1;\psi)x(t_2;\psi_k)\rangle_\psi\,\mathrm{e}^{-\mathrm{j}\omega t_2}\end{aligned} \tag{17}$$

where $\omega = 2\pi\nu$. This expression can be approximated by noticing that the contributions for $t_1 \simeq t_2$ correspond to the highest covariance, since for t_1 significantly different from t_2 the signals $x(t_1;\psi)$ and $x(t_2;\psi_k)$ will diverge, because a lag k implies different propagation scenarios. Moreover, for $t_1 \neq t_2$ the two complex exponentials in (17) will add up increasingly different phase-shift angles, leading to an incoherent summation, which can be expected to be negligible compared to the coherent one for $t_1 = t_2$.

Under these assumptions,

$$\begin{aligned}&\langle x^\star(t_1;\psi)x(t_2;\psi_k)\rangle_\psi \simeq \langle x^\star(t_1;\psi)x(t_1;\psi_k)\rangle_\psi\,\delta(t_1-t_2) \\ &= R(t_1;k)\left\langle|x(t_1;\psi)|^2\right\rangle_\psi\delta(t_1-t_2)\end{aligned} \tag{18}$$

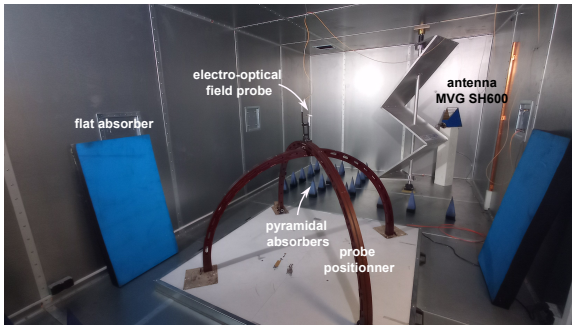

Fig. 3: The setup used during the experiments. Further pyramidal absorbers were also placed on the other half of the RC not visible in the picture.

and recalling (15) and (10)

$$\langle x^\star(\nu;\psi)x(\nu;\psi_k)\rangle_\psi \simeq \int_0^\infty \mathrm{d}t_1\, R(t_1;k)\left\langle |x(t_1;\psi)|^2\right\rangle_\psi$$
$$= \int_0^\infty \mathrm{d}t\, I_t(0)\mathrm{e}^{-t/\tau_s(k)}\mathrm{e}^{-t/\tau_a} = I_t(0)\frac{\tau_a\tau_s(k)}{\tau_a+\tau_s(k)}. \tag{19}$$

Following a similar procedure

$$\left\langle |x(\nu;\psi)|^2\right\rangle_\psi \simeq I_t(0)\tau_a, \tag{20}$$

finally yielding

$$R(\nu,k) \simeq \frac{R_s(\nu,k)\tau_s(\nu,k)}{\tau_a(\nu)+\tau_s(\nu,k)} \tag{21}$$

Sec. IV confirms that (21) accurately predicts the fACF for varyin loading conditions. Further practical implications of (21) are discussed in Sec. V.

Two limit cases can be identified. For low losses, with $\tau_s(\nu,k) \ll \tau_a(\nu)$,

$$R(\nu,k) \simeq R_s(\nu,k)\tau_s(\nu,k)/\tau_a(\nu), \tag{22}$$

where the product of the initial correlation and stirring coherence time controls the stirrer efficiency. For high losses, with $\tau_s(\nu,k) \gg \tau_a(\nu)$,

$$R(\nu,k) \simeq R_s(\nu,k), \tag{23}$$

where the initial coherence R_s controls the stirrer efficiency, since losses now limit the access to the late-time stirrer contribution.

IV. Experimental results

In order to check the validity and accuracy of the theoretical results derived in the previous sections, experiments were conducted in a $6.2\times2.5\times3.3\,\mathrm{m}^3$ galvanized-steel reverberation chamber. The RC has a Z-folded stirrer, 0.8 m wide and about 2.2 m high, visible in Fig. 3. A linearly polarized ridged-horn antenna (MVG SH600) was used for exciting the chamber, characterized by a reflection coefficient lower than -10 dB above 600 MHz; at lower frequencies the higher reflection was compensated during the post-processing of the experimental results. A linearly polarized electro-optical probe (Enprobe EFS-105) was installed around the center of the RC, sampling the vertical component of the electric field. The antenna pointed towards the corner of the RC behind the stirrer, in order to minimize the line-of sight coupling. For the same reason the antenna was set to radiate along an horizontal polarization orthogonal to that of the field probe.The linearly polarized probe was mounted on top of a glass-fiber positioning system, not operated during the experiments, which has negligible perturbation on wave propagation below 3 GHz [32].

#.	Empty RC	#	Mockup EUT
1	unloaded	8	unloaded
2	3 pyramidal abs	9	6 pyramidal abs
3	6 pyramidal abs	10	24 pyramidal abs
4	12 pyramidal abs	11	36 pyram. + 2 flat abs
5	24 pyramidal abs	12	2 flat abs on EUT
6	36 pyramidal abs		
7	36 pyram. + 2 flat abs		

TABLE I: Loading configurations tested in Sec. IV.

The experiments were meant to validate two points. First, that the coherence loss introduced by the stirrer interactions results, over time, into an exponentially decaying tACF, with a stirring coherence function independent from the RC loading. Second, that the fACF of the stirrer-generated field samples in a loaded RC can be effectively predicted for the stirrer tACF estimated in an unloaded RC, by means of (21).

With these objectives in mind, seven loading configurations were initially tested in the empty RC, distributing an increasing number of absorbers across the RC, as detailed in Table I. The complex transfer function $H(\nu;\psi)$ between the antenna and the probe was measured over 8000 frequency samples between 0.4 and 2.0 GHz for each loading configuration, repeating the measurements for 100 stirrer positions ψ, using 3.6 degree steps. Overmoded conditions can be expected to hold above 650 MHz for the unloaded configuration, since the average number of overlapping modes $M_w > 3$ [33], [34], given that

$$M_w(f_c) = 8\pi V_\lambda/Q = 8V_\lambda/f_c\tau_a \tag{24}$$

with $V_\lambda = V/\lambda^3$ and $Q = 2\pi f_c\tau_a$ the composite quality factor, where τ_a is the attenuation time constant (cf. Sec. II). This condition is met at lower frequency as the loading increases. In fact, overmoded conditions are not required in the derivations in Secs. II and III, as confirmed by the results in this section.

For each load configuration we computed the power-delay profile (PDP) $P(t)$

$$P(t;f_c) = \left\langle |h(t,f_c;\psi)|^2\right\rangle_\psi = P_o\mathrm{e}^{-t/\tau_a} \tag{25}$$

averaging over the stirrer-generated samples, depending on its angular position ψ. The impulse responses $h(t,f_c;\psi)$ were obtained by inverse Fourier-transforming $H(\nu;\psi)$ over a 50 MHz bandwidth centered at the frequency f_c. Fig. 4(a) shows the results obtained for $f_c = 1$ GHz. The attenuation time constant τ_a was then estimated by applying a linear regression of the PDP, yielding the results in Fig. 4(b), showing a ten-fold reduction of τ_a passing from the unloaded configuration #1 to the highest load #7. The fact that τ_a is almost independent from the frequency for the unloaded configuration is explained by the fact that galvanized steel-plate walls have a quality

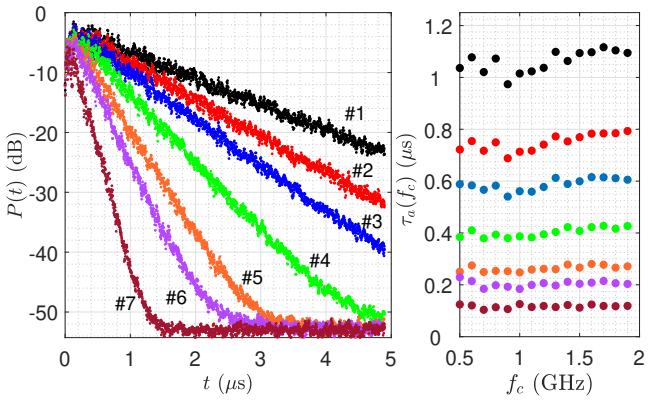

Fig. 4: RC losses: (a) power-delay profile of the signals received by the probe for configurations #1-#7, computed at 1 GHz and (b) attenuation time constants τ_a versus frequency.

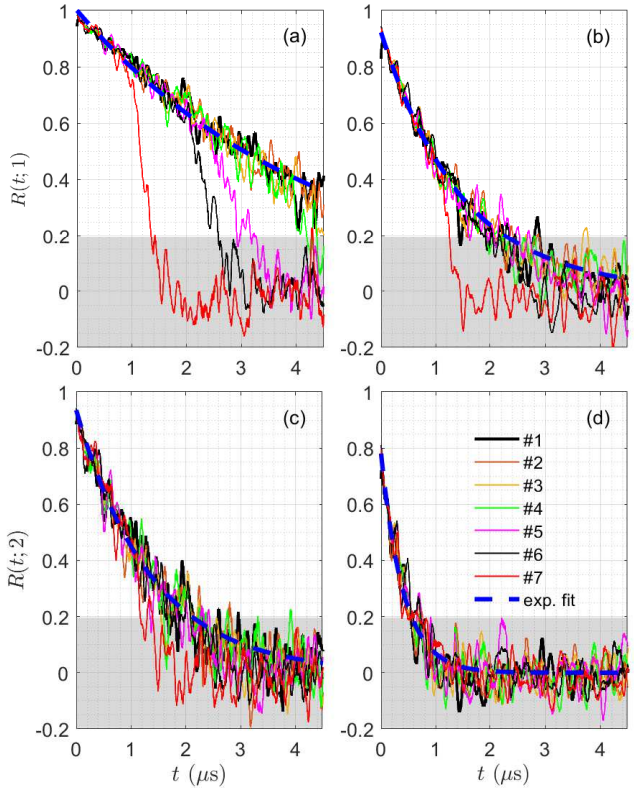

Fig. 5: Evolution of the tACF of the probe output signal, for lag 1 (top row) and lag 2 (bottom row), at 0.5 GHz (left column) and 1.2 GHz (right column). The shaded area represents the 95 % confidence interval for the sample correlation coefficient estimated from 100 i.i.d. samples, under the null hypothesis of zero correlation.

factor proportional to the frequency [35], [36]. A similar frequency independence is expected for absorbers [37].

The tACF $R(t;k)$ of stirrer-generated field samples was computed, according to (11), for a lag $k \in [1,5]$. Results for $k = 1, 2$ in Fig. 5 confirm that $R(t;k)$ closely agrees with an exponential decay, independently from the RC loading and sample lag order k. Exceptions appear at 0.5 GHz for #5, #6 and #7 in Fig. 5(a), where the 1-lag tACF suddenly drops

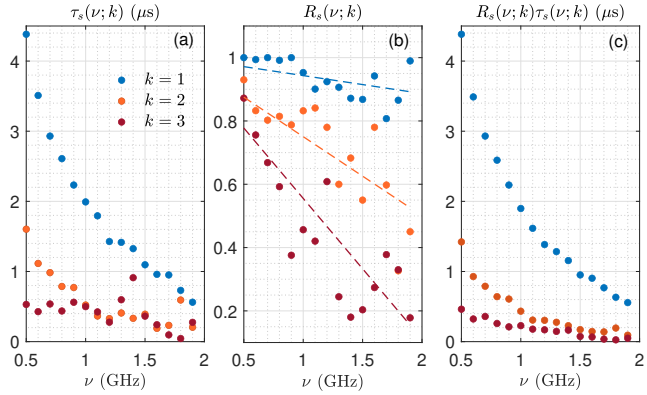

Fig. 6: Stirring coherence parameters estimated from the unloaded RC measurements: (a) stirring coherence time $\tau_s(\nu;k)$; (b) initial coherence $R_s(\nu;k)$; (c) product of the two previous quantities. Lines in Fig. 6(b) represent linear regressions enforcing $R_s(0;k) = 1$.

within the confidence interval expected for a zero-correlation estimated from a population of 100 samples (see Appendix). These results are explained by the higher losses, with τ_a respectively about 200 and 125 ns for case #6 and #7 (cf. Fig. 4(b)), leading to a signal dominated by thermal noise after 1.5 and 2.5 μs for these two cases and therefore a zero correlation.

Fig. 5(b) shows how the exponential decay in the 1-lag tACF is steeper at 1.2 GHz compared to 0.5 GHz, which is consistent with the transport-theory interpretation discussed in Sec. II, since the stirring coherence time τ_s is expected to be directly controlled by the angular correlation of the stirrer scattering pattern, which can be expected to be more directive at higher frequency. In Fig. 6(a) τ_s passes from 4.4 μs for $f_c = 0.5$ GHz to about 1.4 μs at 1.2 GHz, therefore leading to a tACF already within the zero-correlation confidence interval after 2.5 μs. Fig.5(c-d) show that for a lag $k = 2$ the tACF falls within the zero-correlation interval much faster, with a stirring coherence time reduced to 1.6 μs at 0.5 GHz and 0.4 μs at 1.2 GHz, as shown in Fig. 6(a). Estimates of τ_s for lags $k > 3$ are not robust above 1.2 GHz, because of very short coherence times rapidly heading within the zero-correlation zone.

It is interesting to cast τ_s in terms of the average number of interactions with the stirrer. Estimating the average mean-free path within the RC as $\ell = \sqrt[3]{V} \simeq 3.7$ m, with V the RC volume, the mean-free time is about 12.3 ns, indicating that at 0.5 GHz waves propagating through the RC must interact more than 350 times with the stirrer before the 1-lag tACF is reduced by a factor $1/\mathrm{e}$. At 1.2 GHz this requirement drops to 110 interactions. These results show that at 0.5 GHz the 1.6 wavelength-wide stirrer introduces disorder slowly, but over the course of a few microseconds it surely leads to low correlation.

According to (15), the stirring tACF is not only explained by its coherence time but also by the initial coherence $R_s(\nu;k)$. Fig 6(b) shows that while $R_s(\nu;1)$ stays close to one even above 1 GHz, for higher lags it drops much faster, effectively

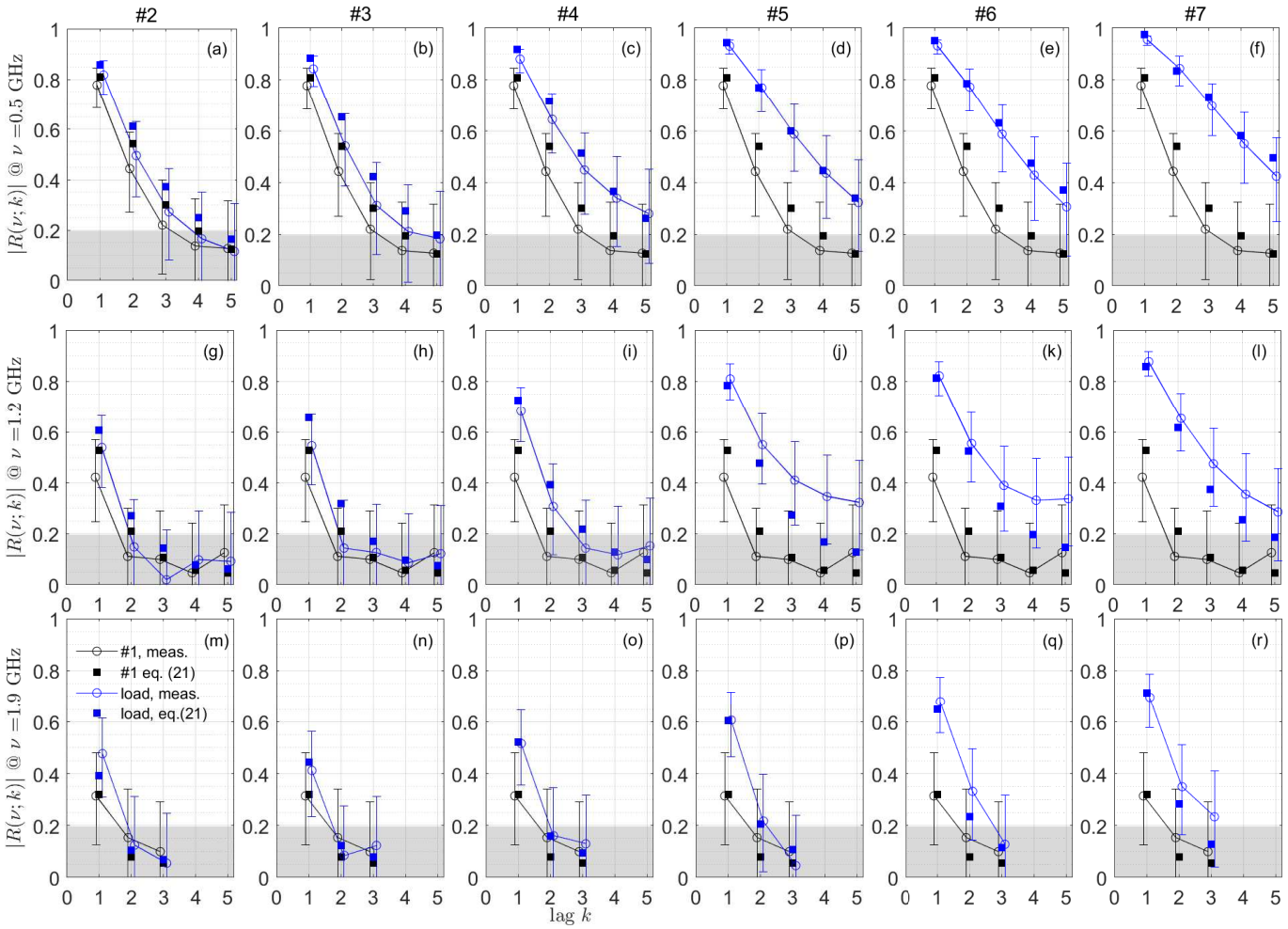

Fig. 7: The fACF of the samples generated by the stirrer, evaluated at 0.5 GHz (top row), 1.2 GHz (middle row) and 1.9 GHz (bottom row), for a maximum lag equal to five, apart for 1.9 GHz, where only lags up to three are shown, since the estimation of the coherence time becomes less robust due to the much faster coherence loss at high frequency . Each column corresponds to a different loading case. Results estimated from experimental data are shown with their 95 % confidence interval. Squares indicate the fACF predicted from (21), based on the stirring coherence coefficients for the unloaded chamber and the attenuation time of each loaded configuration. The shaded area represents the 95 % confidence interval for the sample correlation coefficient estimated from 100 i.i.d. samples, under the null hypothesis of zero correlation.

setting the maximum bound for the tACF, as discussed at the end of Sec. III. Linear regressions of $R_s(\nu;k)$ in Fig. 6(b) clearly show the faster decrease of $R_s(\nu;k)$ versus the frequency. The linear regressions have been set to converge to one at low frequency, since any stirrer will ultimately be unable to provide any loss of coherence as it becomes electrically small.

Fig. 6(c) shows that estimates of the product $R_s(\nu;k)\tau_s(\nu;k)$ are more robust than $R_s(\nu;k)$ alone. This has practical importance, since Sec. III showed that this product controls the stirring efficiency for low-dissipation losses.

Finally, the fACF $R(\nu;k)$ was computed from the measured data, since it is the actual quantity of interest when assessing the stirring efficiency. The results of this operation are shown in Fig. 7 for three frequencies: 0.5, 1.2 and 1.9 GHz. The fACF estimated from measurements for each load are shown in blue, with their 95 % confidence interval, computed as detailed in the Appendix. The original results for the unloaded case, shown in black, serve as a reference, confirming the steady increase in the fACF for a loaded RC. Therefore, a higher angular lag is needed under higher loading conditions, in order to maintain a low fACF, thus reducing the stirring efficiency.

The fACF was also estimated by applying (21), which only requires knowledge of the stirring coherence parameters R_s and τ_s, as well as the attenuation time τ_a, which depends on the RC loading. The results predicted for each loading configuration are shown as blue squares in Fig. 7; black squares are for the unloaded RC case. It appears that (21) accurately predicts the increase in the fACF for all cases considered. Its main advantage is that it only requires knowledge of the two stirring coherence parameters, which do not depend on the loading and can therefore be estimated once for all for different frequencies and stirrer angular step. Given the expected attenuation time τ_a, the fACF is readily estimated.

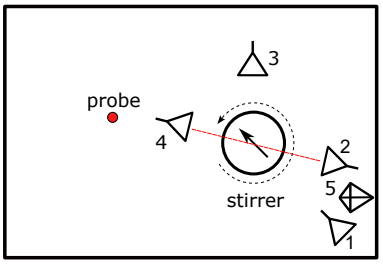

Fig. 8: Source positions tested, with a MVG SH600 ridged-horn antenna (1 to 4) and a top-hat monocone antenna perpendicular to the wall (5). Case 1 was used throughout configurations #1 to #7.

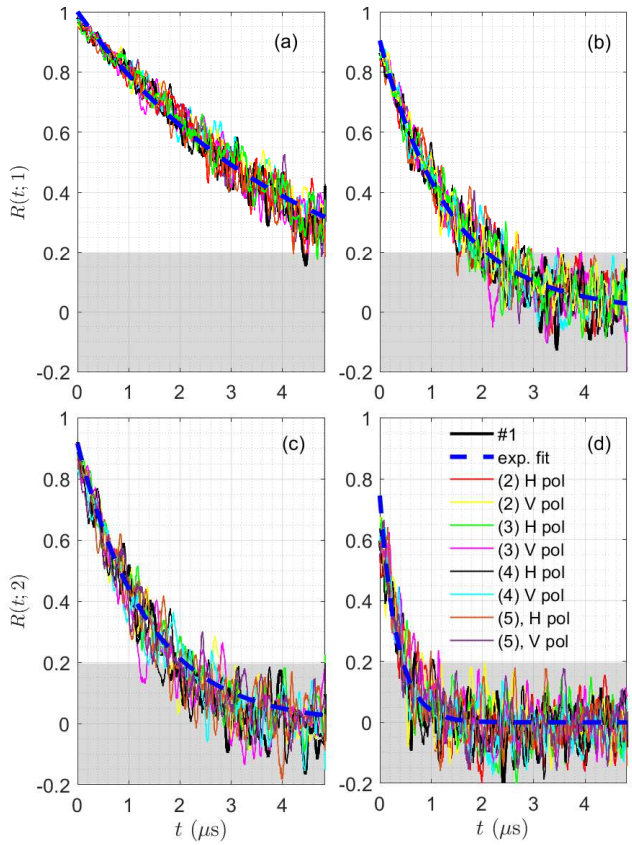

Fig. 9: Comparison of the stirring tACF estimated for different source antennas and positions in the unloaded RC, as defined in Fig. 8. For the monocone antenna (5), the probe orientation was changed, instead of the antenna. Refer to Fig. 5 for the tACF of the empty unloaded RC.

A. Source position

Tests were repeated for the unloaded RC, changing the position of the horn antenna, as shown in Fig. 8, in order to assess if it would impact the initial coherence $R_s(k)$, since the shortest path between the source antenna and the probe would involve significant differences in the angles of scattering from the stirrer, with case (2) involving the forward-scattering and (4) the back-scattering directions. For each position tests were repeated with the horn horizontally and vertically polarized. A hat-topped monocone antenna, with an input matching better than -10 dB above 0.7 GHz, was also tested in case (4): in this case the probe was also oriented vertically. The objective was to check how its omni-directional radiation would affect the estimation of the stirring coherence response, since it would interact with the stirrer across a larger fan of directions. Fig. 9 proves that there is no major difference in the results with these five different configurations. Therefore, similar estimates are obtained for $R_s(k)$ and $\tau_s(k)$.

Fig. 10: The mock-up EUT used during the experiments described in Sec. IV-B.

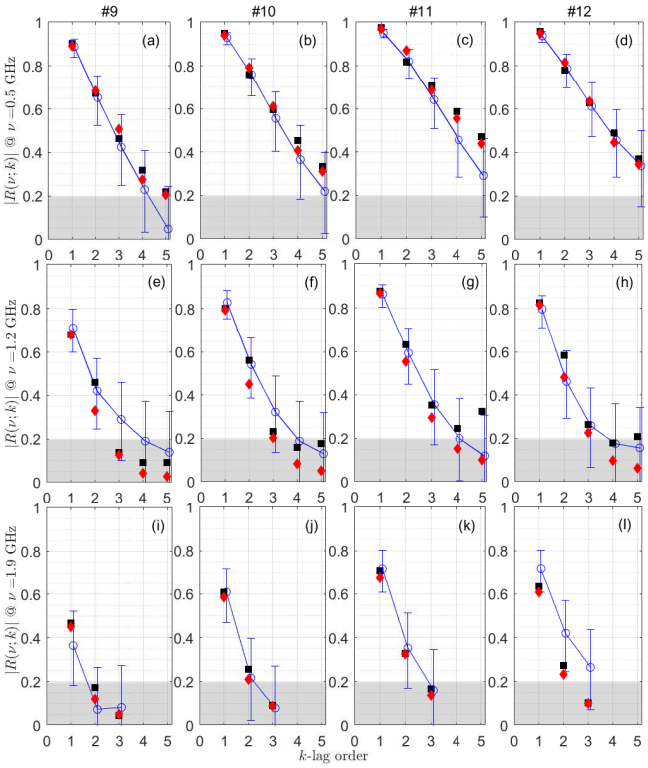

Fig. 11: Comparison of fACF estimated for the loaded RC cases #9 to #12 from data collected from unloaded RC with (red diamonds) and without EUT (black squares).

B. Electrically large EUT

Previous results have dealt with an empty RC, with the stirrer as the only scatterer. Such configuration can serve as a basis for testing small EUTs, such as wireless communication devices, which would have a relatively minor impact on wave propagation. But in case of electrically large EUTs, they would

heavily affect wave propagation. Further experiments were thus carried out in order to asses if the stirring coherence response estimated in an empty RC is still valid even with a large EUT. Indeed, a large EUT amounts to a new scatterer which, from the image-principle point of view, would take part to the diffusion process. Our hypothesis is that this should not affect the stirrer coherence response, since only scattering events with the stirrer introduce coherence loss (see Sec. II-B), with only forward-propagating paths contributing at the probe. Instead, energy scatterer by the EUT will only be diffused, therefore not lost.

A mock–up EUT was introduced in the RC, built by covering with aluminium foil a $50 \times 50 \times 118$ cm^3 block of styrofoam, as shown in Fig. 10. The horn antenna was still in the same initial position used during the first experiments, as well as the field probe. The module of the correlation between the probe signals received with and without the EUT yielded 0.29, 0.18 and 0.032 at 0.5, 1.2 and 1.9 GHz, respectively, confirming the significant impact of the EUT as a scatterer.

Five loading configurations were tested, as detailed in the right column of Table I. The last one involved placing the two flat absorbers directly on the opposite vertical sides of the EUT, in order to emulate a lossy EUT, instead of losses introduced to control the reverberation level. The fACF was computed for each configuration. The stirring coherence function was estimated from the tACF for the unloaded case #8 including the EUT.

The fACF was then predicted by means of (21), using the stirring coherence parameters estimated from the unloaded configurations with and without the EUT. Results in Fig. 11 show that the fACF is accurately predicted from both estimates of the stirring coherence parameters and in particular that it is possible to use the results obtained in the empty RC to predict the stirrer performance in presence of an EUT.

V. Maximum acceptable loading

The ability of (21) to predict the fACF has direct practical implications, since it makes it possible to estimate the maximum acceptable load in order to ensure a maximum acceptable fACF, i.e., $R(\nu) < r$. Recalling that the composite quality factor is $Q = 2\pi f_c \tau_a$, it follows from (21) that

$$\tau_a/\tau_s > R_s/r - 1 \tag{26}$$

or, in terms of the RC quality factor

$$Q > 2\pi f_c \tau_s (R_s/r - 1). \tag{27}$$

In case $r > R_s$, ideally any loading condition could be applied, at least from the point of view of the field fACF, since for heavy loading conditions the fACF is bound by R_s (cf. Sec. III). Other figures of merit as field uniformity may provide limitations to the maximum loading. In all other cases, the maximum loading will depend from both R_s and τ_s.

Eq. (21) is also useful in estimating the effective number of independent samples generated by a stirrer undergoing N steps. Based on the first-order auto-regressive model discussed in [4], the effective number N_e of independent samples generated by a stirring process with an fACF r is

$$N_e = N(1-r)/(1+r) \tag{28}$$

from which

$$(N - N_e)/N = 2r/(1-r) \tag{29}$$

which is the relative increment in the number of tests to run, having invested time to carry out N measurements that in practice correspond to only N_e independent results. In order to keep $(N - N_e)/N$ below a threshold p, it is necessary that

$$\tau_a/\tau_s > R_s(1 + 2/p) - 1. \tag{30}$$

These two results show how the stirring coherence time τ_s and the initial coherence R_s are an effective and practical figures of merit for the characterization of a stirrer. Clearly, they could as well be used in order to assess if a given stirrer (or an RC) is well suited to testing an EUT of which the loading, and therefore τ_a, is already known.

Similar results can be derived in order to bind the stirring coherence parameters to the correlation of the received power, instead of the complex signal received by the probe. In this case (21) will first need to be squared, as proven in [31].

VI. Conclusions

This paper has presented a new interpretation of how mechanical stirrers affect the field distribution within a reverberation chamber (RC), based on a model inspired by transport theory, which provides a natural framework for explaining the time evolution of diffusive phenomena. This model clearly shows that the frequency-domain auto-correlation function (fACF) of field samples generated by the stirrer is controlled by two independent time constants: the stirring coherence time, modelling the ability of the stirrer to introduce disorder, and the power decay time of the RC.

These results prove that a stirrer efficiency under any loading condition can be predicted from the time-domain auto-correlation function (tACF) estimated under unloaded conditions. As a consequence, the maximum acceptable loading that still ensures a minimum required stirring efficiency can be straightforwardly established using the proposed model.

This property is expected to be useful for EMC testing of an equipment under test whose power loss characteristics are known, in order to rapidly assess if the stirring technique will need to be modified, e.g., by increasing the number of stirrer steps. In over-the-air (OTA) tests for wireless communications, RCs are systematically loaded in order to control the complexity of the propagation environment. In this case, too, it would be useful to be able to predict if under different loading conditions the stirring efficiency will still be sufficient to ensure precise testing.

The stirring coherence function could also be used in order to rapidly asses a stirrer efficiency during time-domain numerical simulations. The fact that this function can be computed without waiting for the end of signal transients would significantly reduce the duration of the simulations.

This investigation has also highlighted one important fact: the stirring efficiency is a relative notion, which does not only depend on the stirrer electrical dimensions, but also on the RC volume and power loss. The proposed model avoids and clarifies the confusion arising from the impact of losses on the stirrer efficiency.

Future work will focus on the possibility of predicting from tests on an unloaded RC not only the stirrer efficiency for loaded configurations, but also other fundamental figures of merit of RCs, such as spatial field uniformity and polarization isotropy.

APPENDIX

The sample distribution of the Pearson correlation coefficient $\hat{\rho}$ derived from two populations of N samples with correlation ρ can be approximated by using Fisher's z-transformation $F(x) = \tanh^{-1}(x)$, introducing the auxiliary random variable [38]

$$z = [F(\hat{\rho}) - F(\rho)]\sqrt{N-3} \tag{31}$$

whose probability distribution is very well approximated by a standard gaussian distribution. The confidence interval of $\hat{\rho}$ at α significance can therefore be found by first identifying the quantiles $\pm q_{1-\alpha/2}$ of z, and then deriving the associated quantiles of $\hat{\rho}$, i.e., the bounds of the confidence interval of $\hat{\rho}$, as

$$\tanh\left[\tanh^{-1}(\rho) \pm q_{1-\alpha/2}\sqrt{N-3}\right] \tag{32}$$

REFERENCES

[1] *Testing and measurement techniques - Reverberation chamber test methods*, International Electrotechnical Commission (IEC) Std. 61 000-4-21, 2011.

[2] R. Serra, "Reverberation chambers through the magnifying glass: an overview and classification of performance indicators," *IEEE Electromagn. Compat. Mag.*, vol. 6, no. 2, pp. 76–88, 2017.

[3] R. Serra, A. C. Marvin, F. Moglie, V. M. Primiani, A. Cozza, L. R. Arnaut, Y. Huang, M. O. Hatfield, M. Klingler, and F. Leferink, "Reverberation chambers a la carte: An overview of the different mode-stirring techniques," *IEEE Electromagnetic Compatibility Magazine*, vol. 6, no. 1, pp. 63–78, First 2017.

[4] C. Lemoine, P. Besnier, and M. Drissi, "Estimating the effective sample size to select independent measurements in a reverberation chamber," *IEEE Trans. Electromagn. Compat.*, vol. 50, no. 2, pp. 227–236, May 2008.

[5] R. J. Pirkl, K. A. Remley, and C. S. L. Patane, "Reverberation chamber measurement correlation," *IEEE Trans. Electromagn. Compat.*, vol. 54, no. 3, pp. 533–545, 2012.

[6] O. Lunden and M. Backstrom, "Stirrer efficiency in foa reverberation chambers. evaluation of correlation coefficients and chi-squared tests," in *IEEE Intern. Symp. Electromagn. Compat.. Symposium Record*, vol. 1, 2000, pp. 11–16 vol.1.

[7] P. Hallbjörner, "A model for the number of independent samples in reverberation chambers," *Microwave and optical technology letters*, vol. 33, no. 1, pp. 25–28, 2002.

[8] N. Wellander, O. Lundén, and M. Bäckström, "Experimental investigation and mathematical modeling of design parameters for efficient stirrers in mode-stirred reverberation chambers," *IEEE Trans. Electromagn. Compat.*, vol. 49, no. 1, pp. 94 –103, feb. 2007.

[9] A. Ubin, R. Vogt-Ardatjew, F. Leferink, M. Z. Mohd Jenu, and S. Van De Beek, "Statistical analysis of three different stirrer designs in a reverberation chamber," in *2015 Asia-Pacific Symp. Electromagn. Compat. (APEMC)*, 2015, pp. 604–607.

[10] F. Moglie and V. M. Primiani, "Reverberation chambers: Full 3D FDTD simulations and measurements of independent positions of the stirrers," in *2011 IEEE Intern. Symp. Electromagn. Compat.*, 2011, pp. 226–230.

[11] J.-I. Hong and C.-S. Huh, "Optimization of stirrer with various parameters in reverberation chamber," *Progress In Electromagnetics Research*, vol. 104, pp. 15–30, 2010.

[12] L. Arnaut, "Effect of size, orientation, and eccentricity of mode stirrers on their performance in reverberation chambers," *IEEE Trans. Electromagn. Compat.*, vol. 48, no. 3, pp. 600–602, 2006.

[13] D. Fedeli, M. Iualè, V. M. Primiani, and F. Moglie, "Experimental and numerical analysis of a carousel stirrer for reverberation chambers," in *2012 IEEE Intern. Symp. Electromagn. Compat.*, 2012, pp. 228–233.

[14] Y. Huang, N. Abumustafa, Q. G. Wang, and X. Zhu, "Comparison of two stirrer designs for a new reverberation chamber," in *The 2006 4th Asia-Pacific Conference on Environmental Electromagnetics*, 2006, pp. 450–453.

[15] V. Creta, L. Bastianelli, F. Moglie, V. M. Primiani, and L. R. Arnaut, "Stirring performance of helically distributed paddles," in *2017 IEEE Intern. Symp. Electromagn. Compat. & Signal/Power Integrity (EMCSI)*, 2017, pp. 670–674.

[16] J. Tang, F. Li, J. Zheng, X. Chen, Y. Li, and J. Chen, "A new mode stirrer design for the reverberation chamber," *The Applied Computational Electromagnetics Society Journal (ACES)*, pp. 1182–1188, 2021.

[17] X. Chen, "On independent platform sample number for reverberation chamber measurements," *IEEE Trans. Electromagn. Compat.*, vol. 54, no. 6, pp. 1306–1309, 2012.

[18] A. Adardour, G. Andrieu, and A. Reineix, "Determination of the "quasi-ideal reverberation chamber minimal frequency" according to loading," in *2013 IEEE Intern. Symp. Electromagn. Compat.*, 2013, pp. 213–216.

[19] F. Moglie and V. M. Primiani, "Analysis of the independent positions of reverberation chamber stirrers as a function of their operating conditions," *IEEE Trans. Electromagn. Compat.*, vol. 53, no. 2, pp. 288–295, 2011.

[20] V. Rajamani, C. F. Bunting, and J. C. West, "Effects of loading on independent samples and uniformity of a reverberation chamber," in *2013 IEEE Intern. Symp. Electromagn. Compat.*, 2013, pp. 217–221.

[21] X. Chen, "Experimental investigation of the number of independent samples and the measurement uncertainty in a reverberation chamber," *IEEE Trans. Electromagn. Compat.*, vol. 55, no. 5, pp. 816–824, 2013.

[22] G. Andrieu, N. Ticaud, F. Lescoat, and L. Trougnou, "Fast and accurate assessment of the "well stirred condition" of a reverberation chamber from S_{11} measurements," *IEEE Trans. Electromagn. Compat.*, vol. 61, no. 4, pp. 974–982, 2019.

[23] Q. Xu, Y. Huang, L. Xing, Z. Tian, C. Song, and M. Stanley, "The limit of the total scattering cross section of electrically large stirrers in a reverberation chamber," *IEEE Trans. Electromagn. Compat.*, vol. 58, no. 2, pp. 623–626, 2016.

[24] S. Lalléchère, I. El Baba, P. Bonnet, and F. Paladian, "Total scattering cross section improvements from electromagnetic reverberation chambers modeling and stochastic formalism," in *Proceedings of the 5th European Conf. on Antennas Propag. (EUCAP)*, 2011, pp. 81–85.

[25] Q. Xu, Y. Huang, L. Xing, Z. Tian, M. Stanley, and S. Yuan, "B-scan in a reverberation chamber," *IEEE Trans. Antennas Propag.*, vol. 64, no. 5, pp. 1740–1750, 2016.

[26] G. Lerosey and J. de Rosny, "Scattering cross section measurement in reverberation chamber," *IEEE Trans. Electromagn. Compat.*, vol. 49, no. 2, pp. 280–284, 2007.

[27] A. Ishimaru, *Wave propagation and scattering in random media*. Wiley-IEEE Press, 1999, vol. 12.

[28] H. Kuttruff, *Room acoustics*. Taylor & Francis, 2000.

[29] E. Amador, C. Lemoine, P. Besnier, and A. Laisné, "Reverberation chamber modeling based on image theory: Investigation in the pulse regime," *IEEE Trans. Electromagn. Compat.*, vol. 52, no. 4, pp. 778–789, 2010.

[30] J.-D. Polack, "Playing billiards in the concert hall: The mathematical foundations of geometrical room acoustics," *Applied Acoustics*, vol. 38, no. 2, pp. 235–244, 1993.

[31] F. Monsef, A. Cozza, and R. Serra, "Linking lag-1 correlation coefficients between field-related quantities in a reverberation chamber," *IEEE Trans. Electromagn. Compat.*, vol. 62, no. 4, pp. 1358–1360, 2020.

[32] A. Cozza, F. Masciovecchio, C. Dorgan, M. Serhir, F. Monsef, and D. Lecointe, "A dielectric low-perturbation field scanner for multi-path environments," *IEEE Trans. Antennas Propag.*, vol. 65, no. 4, pp. 1978–1987, April 2017.

[33] A. Cozza, "The role of losses in the definition of the overmoded condition for reverberation chambers and their statistics," *IEEE Trans. Electromagn. Compat.*, vol. 53, no. 2, pp. 296–307, May 2011.

[34] F. Monsef and A. Cozza, "Average number of significant modes excited in a mode-stirred reverberation chamber," *IEEE Trans. Electromagn. Compat.*, vol. 56, no. 2, pp. 259–265, 2014.

[35] A. Cozza and F. Monsef, "Power dissipation in reverberation chamber metallic surfaces based on ferrous materials," *IEEE Trans. Electromagn. Compat.*, vol. 61, no. 6, pp. 1714–1725, 2018.

[36] A. Cozza, "Understanding the apparently poor conductivity of galvanized steel plates," *IEEE Access*, vol. 9, pp. 146 625–146 639, 2021.

[37] D. A. Hill, *Electromagnetic fields in cavities: deterministic and statistical theories*. John Wiley & Sons, 2009.

[38] N. J. Salkind, *Encyclopedia of measurement and statistics*. SAGE publications, London, 2006.